Nonnodal Extended Finite-Element Method for Crack Modeling with Four-Node Quadrilateral Elements

Iman Asareh[1] and Jeong-Hoon Song, M.ASCE[2]

Abstract: A nonnodal extended finite-element method (NXFEM) was developed to predict two-dimensional dynamic failure with four-node quadrilateral elements. A new nonnodal enrichment scheme is presented such that the enriched quadrilateral finite elements satisfy the linear completeness and represent a strong discontinuity, i.e., crack. The enrichment bases for both solutions and the gradient fields are included in the finite-element approximation through the nonnodal enrichment scheme. The partition of unity is also naturally satisfied without adopting additional neighbor blending elements. To facilitate an implementation of the NXFEM into pre-existing finite-element analysis software, a generalized notation is proposed which is universally applicable to both quadrilateral and triangular finite elements. The developed method was initially verified with a convergence study on benchmark near-crack-tip field problems. The effectiveness of the method was further demonstrated with mixed-mode dynamic failure problems. **DOI: 10.1061/(ASCE)EM.1943-7889.0001662.** *© 2019 American Society of Civil Engineers.*

Author keywords: Nonnodal enrichment; Linear completeness; Strong discontinuity; Dynamic fracture.

Introduction

Since the extended finite-element method (XFEM) was first developed by Belytschko and colleagues (Belytschko and Black 1999; Moës et al. 1999), a plethora of computational methods has been developed to model arbitrary weak and strong discontinuities within a finite element without cumbersome remeshing (Song et al. 2006; Song and Belytschko 2009a, b; Chau-Dinh et al. 2012; Lua et al. 2016). This is mainly accomplished by adopting the partition of unity method (Babuška and Melenk 1997; Melenk and Babuška 1996) whereby the nonpolynomial enrichment bases, which are often called enrichment functions, are associated with enrichment parameters and added to a local finite-element approximation. These enrichment functions are selected to reflect the nature of discontinuities; for instance, a step function for the representation of strong discontinuity (Moës et al. 1999), crack-tip functions for modeling asymptotic crack-tip stress singularity (Belytschko and Black 1999; Wang and Waisman 2017), and a distance function for weak discontinuities along a material interface (Belytschko et al. 2001; Sukumar et al. 2001). Moreover, Song et al. (2006) introduced the phantom node method to model the arbitrary discontinuities with consistent history variables. As alternative classes of methods, the cracking-particle method (Rabczuk and Belytschko 2004; Rabczuk et al. 2010) and efficient remeshing algorithms (Areias et al. 2018; Areias and Rabczuk 2017; Areias et al. 2013, 2016) have been successfully introduced in crack modeling. The XFEM has also been successfully adopted in multiscale failure problems (Tabarraei et al. 2013; Song and Yoon 2014; Sun et al. 2014).

[1]Research Assistant Professor, Dept. of Civil and Environmental Engineering, Univ. of South Carolina, Columbia, SC 29208. ORCID: https://orcid.org/0000-0001-6993-6614

[2]Assistant Professor, Dept. of Civil, Environmental, and Architectural Engineering, Univ. of Colorado Boulder, Boulder, CO 80309 (corresponding author). ORCID: https://orcid.org/0000-0002-2932-440X. Email: jh.song@colorado.edu

Note. This manuscript was submitted on October 5, 2018; approved on March 13, 2019; published online on August 6, 2019. Discussion period open until January 6, 2020; separate discussions must be submitted for individual papers. This paper is part of the ***Journal of Engineering Mechanics***, © ASCE, ISSN 0733-9399.

However, several difficulties arise in adopting the conventional XFEM for practical engineering problems. One of the main difficulties is that the interpretation of enrichment parameters is difficult, which renders the imposition of nonsmooth boundary constraints (Dolbow et al. 2000) and interface constraints (Dolbow et al. 2001; Kim et al. 2007) difficult. These constraints are often enforced in the weak form using Lagrange multiplier techniques. Another difficulty is that in the conventional XFEM, some finite-element nodes may not be enriched due to C^0 continuity conditions between the enriched element and its contiguous elements (Fries and Belytschko 2010); these elements are often called blending elements and are required to be treated appropriately (Chessa et al. 2003; Fries 2008).

To circumvent these difficulties, the nonnodal extended finite-element method (NXFEM) (Asareh et al. 2018a, b) was proposed by adopting additional enrichment nodes independent of the pre-existing finite-element nodes. The ideas for using nonnodal enrichment within a similar context were initially proposed in previous studies (Soghrati et al. 2012; Aragón and Simone 2017); the interface-enriched generalized finite-element method (Soghrati et al. 2012) introduced the concept of associating enriched degrees of freedom with element edges, and the subsequent discontinuity-enriched finite-element method (Aragón and Simone 2017) adopted both strong and weak discontinuous enrichment functions within the same framework. However, the motivation and the formalism for constructing enrichment functions are distinct between these methods. Although the NXFEM can be still considered as yet another variation of the standard XFEM, the major difference is that the enrichment bases are associated with physically based enrichment parameters and assigned to a set of nonnodal points on the crack interface. Because the enrichment parameters are physically based quantities, the Dirichlet boundary conditions on the interface can be simply incorporated in the strong form. However, in the NXFEM, because a local partition of unity is not generically constructed, the enrichment functions must be enforced to satisfy C^0 continuity conditions, which can be viewed as one of the major challenges arisen in developing enrichment schemes for the NXFEM.

The main objective of this study was to develop nonnodal enrichment functions for two-dimensional quadrilateral elements

for both strong and weak discontinuities, i.e., a linear complete element. In this study, the new enrichment functions for quadrilateral element were chosen to include the predeveloped NXFEM's enrichment functions for three-node triangular elements (Asareh et al. 2018a). This implies that a crack can be naturally modeled with a unified scheme for both quadrilateral and triangular elements, which significantly simplifies the implementation of the NXFEM into a general finite-element library.

The remainder of this paper is organized as follows. First, the nonnodal enrichment functions are presented for two-dimensional four-node quadrilateral elements. Then the weak form and discretized equations are provided for dynamic failure analysis. After briefly summarizing the time-stepping algorithm used in this study, the performance of the method is verified with numerical examples including convergence studies of the NXFEM with crack-tip fields and mixed-mode dynamic failure problems. Finally, future directions and conclusions are presented.

Representation of Crack for Four-Node Quadrilateral Elements with Nonnodal Enrichment Scheme

Consider a two-dimensional domain Ω in configuration shown in Fig. 1(a). The body is allowed to contain arbitrary strong discontinuity, i.e., crack denoted by Γ_c. To describe the crack geometry, level set functions (Adalsteinsson and Sethian 1995; Sethian 1996) are adopted. In this approach, the sides of the crack are signed by a continuous level set function $f(\mathbf{X})$ so that $f = 0$ describes the topology of crack surface. The level-set function f can be described by a signed distance function as

$$f(\mathbf{X}) = \min_{\bar{\mathbf{X}} \in \Gamma_c} \|\mathbf{X} - \bar{\mathbf{X}}\| \text{sign}(\mathbf{n}^+(\bar{\mathbf{X}} - \mathbf{X})) \tag{1}$$

where $\bar{\mathbf{X}}$ = closest point on the interface to $\mathbf{X}$; $\|\cdot\|$ is the Euclidean norm; and $\mathbf{n}^+$ = normal to the crack surface where the sign function is positive. In conjunction with the function f, another level set function $g(\mathbf{X}, t)$ is also defined so that the crack is contained within the subdomain $g > 0$; details were given by Ventura et al. (2003).

In the NXFEM (Asareh et al. 2018b), a scalar component of the discontinuous displacement fields is described by

$$u(\mathbf{X}) = u^{\text{cont}}(\mathbf{X}) + u^{\text{disc}}(\mathbf{X}) = \sum_{I \in \delta} N_I(\mathbf{X}) u_I + \sum_{K \in \varepsilon} \sum_{J \in \delta_{\text{NP}}^K} \Psi_J^K(\mathbf{X}) a_J^K \tag{2}$$

where δ = entire set of finite-element nodes within the computational domain; and ε = set of types of enrichment functions, which is defined at the set of additional nonnodal degree of freedoms δ_{NP}^K; for the enrichment function K at the nonnodal point J, the enrichment function and its associated physically based enrichment parameter are denoted by Ψ_J^K and a_J^K, respectively.

In the NXFEM, to represent a strong discontinuity across the crack interface, first a physically based enrichment parameter which can best reflect the characteristics of the discontinuity is selected. Then the enrichment functions Ψ_J are constructed for the discontinuous function Φ^K within finite elements so that they satisfy the following equations (Asareh et al. 2018b):

$$\sum_{I \in \delta_n^-} N_I [\![\Phi^K]\!]_{\mathbf{X}=\mathbf{X}_I} = \sum_{J \in \delta_{\text{NP}}^K} \Psi_J^{K+} \mathbf{a}_J^K$$
$$\sum_{I \in \delta_n^+} -N_I [\![\Phi^K]\!]_{\mathbf{X}=\mathbf{X}_I} = \sum_{J \in \delta_{\text{NP}}^K} \Psi_J^{K-} \mathbf{a}_J^K \tag{3}$$

where $[\![\Phi]\!]_{\mathbf{X}=\mathbf{X}_I}$ = magnitude of jump in discontinuous function at element node I across the strong discontinuity, i.e., $[\![\Phi]\!]_{\mathbf{X}=\mathbf{X}_I} = \Phi^+(\mathbf{X}_I) - \Phi^-(\mathbf{X}_I)$; and δ_n^+ and δ_n^- = sets of finite-element nodes on subdomains where $f > 0$ and $f < 0$, respectively. These sets are defined locally for two different elements in Fig. 1(b). Eq. (3) was developed for a multidimensional multinode finite element when the parts of the discontinuous function on each side of the crack, i.e., Φ^+ and Φ^-, are smooth enough to be interpolated by standard shape functions on the entire element domain (Asareh et al. 2018b). For complex crack patterns such as branching and joining cracks (Bordas et al. 2008), additional nonnodal points must be associated with the intersection points. In addition, to construct enrichment functions using Eq. (3), the C^0 continuity condition between the enriched element and its contiguous elements must be satisfied.

In this study, for enrichment functions Ψ^K, i.e., $K \in \epsilon = \{1, 2\}$, to properly reproduce linear complete fields within the enriched

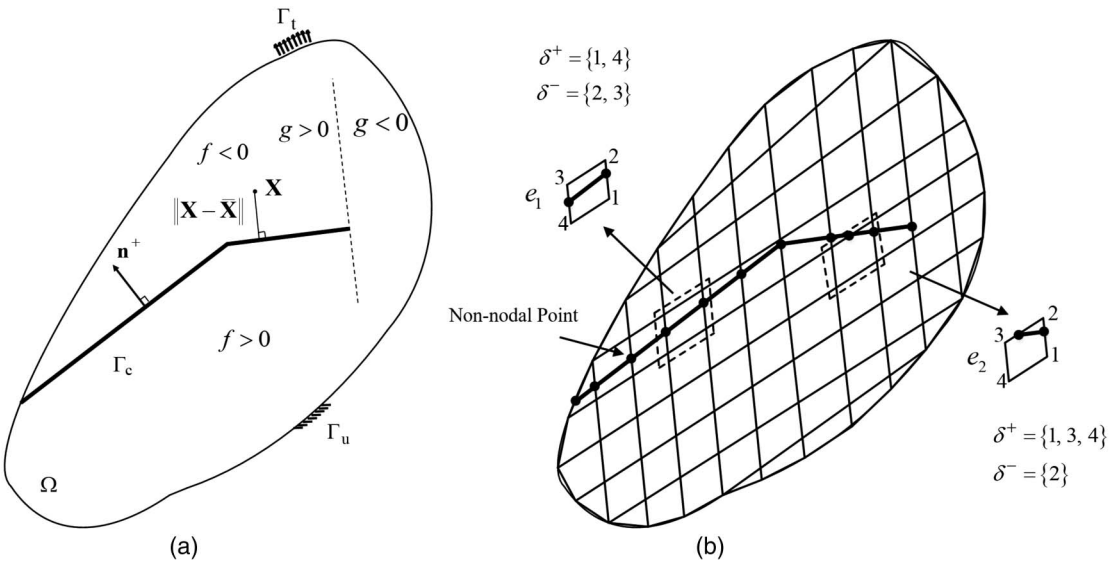

Fig. 1. (a) Two-dimensional body in the current configuration; and (b) schematic of finite-element mesh.

J. Eng. Mech., 2019, 145(10): 04019081

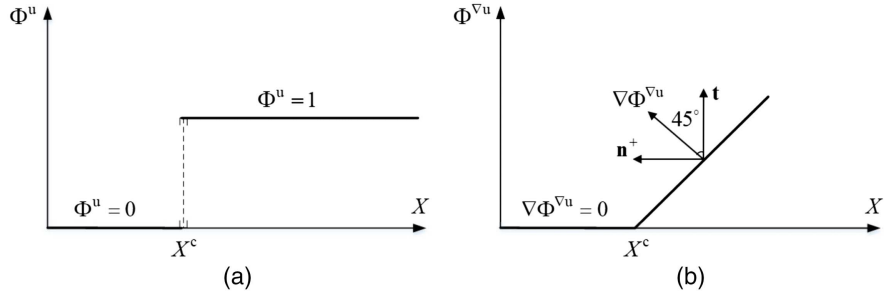

Fig. 2. Representation of the discontinuity in (a) a function, denoted Φ^u; and (b) a derivative of a function, denoted $\Phi^{\nabla u}$. (Modified from Asareh et al. 2018a.)

finite elements (Asareh et al. 2018a). Two types of discontinuous functions were considered: (1) a strong discontinuity $\Phi^{K=1}$ which is associated with the jumps in the interpolated solution fields, and (2) a weak discontinuity $\Phi^{K=2}$ related to the jumps in the derivative of the interpolated solution fields. Henceforth, the set $\epsilon = \{1, 2\}$ is substituted by $\epsilon = \{u, \nabla u\}$ to denote that Φ^u and $\Phi^{\nabla u}$ are discontinuities in the displacement and strain fields, respectively; Φ^u is defined as

$$\Phi^u = H(f(\mathbf{X})) = \begin{cases} 0 & \text{if } f < 0 \\ 1 & \text{if } f > 0 \end{cases} \tag{4}$$

and $\Phi^{\nabla u}$ is defined as

$$\Phi^{\nabla u} = H(f(\mathbf{X})) \times f(\mathbf{X}) = \begin{cases} 0 & \text{if } f < 0 \\ f(\mathbf{X}) & \text{if } f > 0 \end{cases} \tag{5}$$

where $H(\mathbf{X})$ = step function which is adopted to define the discontinuous functions with a unit magnitude on $f > 0$ and zero on $f < 0$; these functions are shown in Fig. 2 in one dimension across the crack at $X = X^c$.

In addition, the specific formalism for the enrichment function that satisfies C^0 continuity within a finite element, i.e., Eq. (3), depends on the relative location of the crack inside the finite element. For example, when the crack passes through nonadjacent edges, i.e., the element e_1 in Fig. 1(b), the original quadrilateral element is partitioned into two quadrilateral subdomains. However, when the crack passes through nonadjacent edges, i.e., the element e_2 in Fig. 1(b), the element is partitioned into a triangular and a pentagonal subdomain. Therefore, the enrichment functions for each case, i.e., for the cases of e_1 and e_2 in Fig. 1(b), must be separately developed according to these two representative locations of crack within a finite element. In the next section, these two cases are distinguished and subsequently the enrichment functions are constructed for (1) the case in which a crack passes through the nonadjacent edges, i.e., e_1, and (2) the case in which the crack passes through adjacent edges, i.e., e_2 in Fig. 1(b).

Enrichment Functions for a Crack Passing through Nonadjacent Edges

Consider a finite element with local node numbers as shown in Fig. 3(a). A straight crack is considered within a finite element which has propagated from the finite-element Edge S_4 to S_2 without changing its propagation angle within the finite element. In this case, the original finite element is partitioned into two rectangular subdomains. The nonnodal points $\mathbf{X}_1^c$ and $\mathbf{X}_2^c$ denote the intersection points between the crack and element edges S_4 and S_2, respectively.

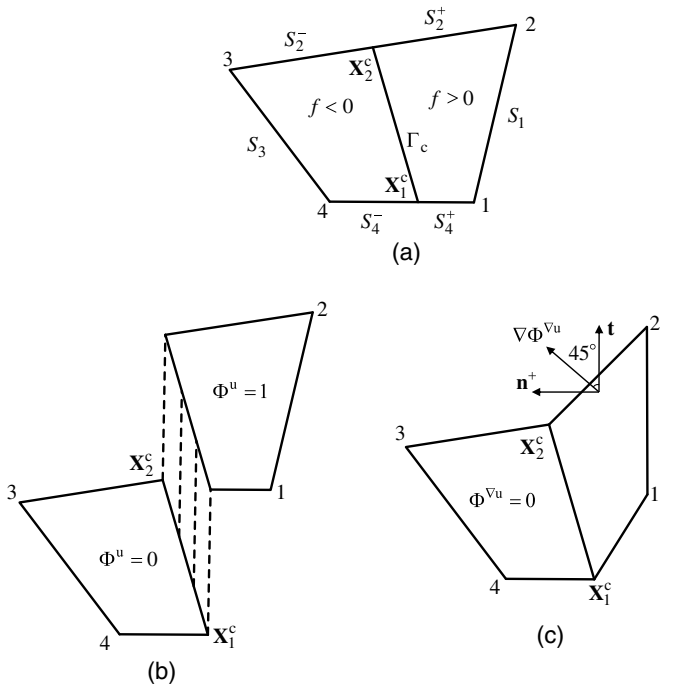

Fig. 3. Representation of a crack for the case when the crack passes through nonadjacent edges: (a) two-dimensional quadrilateral element with a crack; (b) Φ^u; and (c) $\Phi^{\nabla u}$. (Modified from Asareh et al. 2018a.)

For the construction of the enrichment functions for discontinuity in the interpolated solution fields, i.e., Φ^u, the displacement jumps $[\![u]\!]_1$ and $[\![u]\!]_2$ at nonnodal points $\mathbf{X}_1^c$ and $\mathbf{X}_2^c$, respectively, are selected as enrichment parameters [Fig. 3(b)]. For this case, Eq. (3) gives

$$N_3 + N_4 = \Psi_1^{u+} + \Psi_2^{u+} \tag{6a}$$

$$-N_1 - N_2 = \Psi_1^{u-} + \Psi_2^{u-} \tag{6b}$$

The enrichment functions are defined so that they satisfy the C^0 continuity condition among an enriched element and its contiguous elements (Asareh et al. 2018b). In Eq. (6*a*), Ψ_1^{u+} (respectively, Ψ_2^{u+}) must vanish along surfaces S_1 and S_2^+ (respectively, S_1 and S_4^+). Similarly, in Eq. (6*b*), Ψ_1^{u-} (respectively, Ψ_2^{u-}) also has to vanish along surfaces S_3 and S_2^- (respectively, S_3 and S_4^-). Thus, for the representation of discontinuity in the solution fields in Fig. 3(b), the enrichment functions Ψ^u can be described as

J. Eng. Mech., 2019, 145(10): 04019081

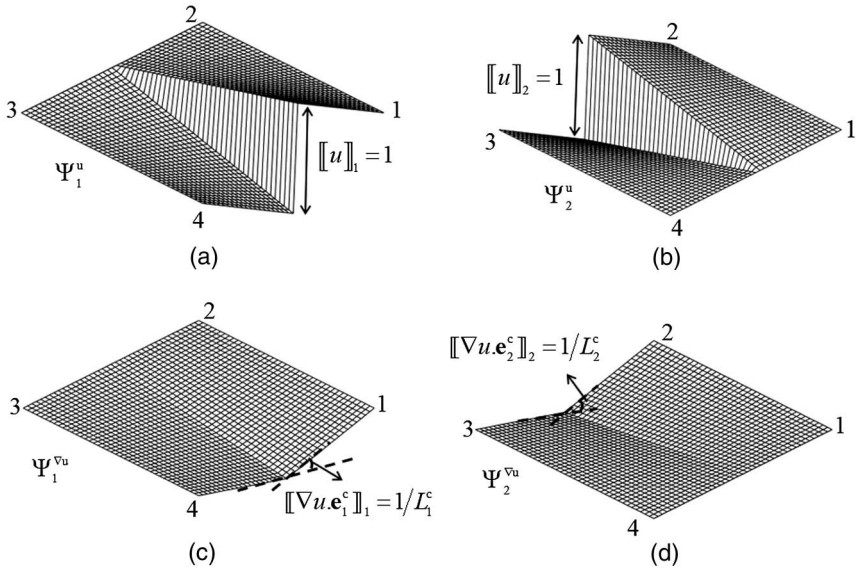

Fig. 4. Enrichment functions for the case when the crack passes through nonadjacent edges: (a) Ψ_1^u; (b) Ψ_2^u; (c) $\Psi_1^{\nabla u}$; and (d) $\Psi_2^{\nabla u}$. (Modified from Asareh et al. 2018a.)

$$\Psi_1^{\mathrm{u}} = \begin{cases} -N_1 & f < 0 \\ N_4 & f > 0 \end{cases} \quad \text{and} \quad \Psi_2^{\mathrm{u}} = \begin{cases} -N_2 & f < 0 \\ N_3 & f > 0 \end{cases} \tag{7}$$

These enrichment functions are shown in Figs. 4(a and b).

For the representation of discontinuity in the derivative of solution fields across the crack interface, i.e., Fig. 3(c), the jumps in directional derivatives of the displacement at the intersection points are chosen as enrichment parameters (Asareh et al. 2018a). To this end, the enrichment functions $\Phi^{\nabla u}$ are constructed from $[\![L_J^c \nabla \mathbf{u} \cdot \mathbf{e}_J^c]\!]_J$, where L_J^c is the length of the element edge that contains the nonnodal point $\mathbf{X}_J^c$, and $\mathbf{e}_J^c$ is a unit vector parallel to the element edge which contains the nonnodal point $\mathbf{X}_J^c$ (Fig. 5); its direction is defined so that $\mathbf{e}_J^c \cdot \mathbf{n}^+ \geq 0$. Therefore, Eq. (3) gives

$$\begin{aligned} -N_3|f_3| - N_4|f_4| &= \Psi_1^{\nabla u+} [\![L_1^c \nabla \Phi^{\nabla u} \cdot \mathbf{e}_1^c]\!]_1 + \Psi_2^{\nabla u+} [\![L_2^c \nabla \Phi^{\nabla u} \cdot \mathbf{e}_2^c]\!]_2 \\ -N_1|f_1| - N_2|f_2| &= \Psi_1^{\nabla u-} [\![L_1^c \nabla \Phi^{\nabla u} \cdot \mathbf{e}_1^c]\!]_1 + \Psi_2^{\nabla u-} [\![L_2^c \nabla \Phi^{\nabla u} \cdot \mathbf{e}_2^c]\!]_2 \end{aligned} \tag{8}$$

where $f_I = f(\mathbf{X}_I)$. The dot products in Eq. (8) can be replaced with the geometric properties by (Fig. 5)

$$[\![\nabla \Phi^{\nabla u} \cdot \mathbf{e}_1^c]\!]_1 = \frac{|f_4|}{L_1^{c-}} \quad \text{and} \quad [\![\nabla \Phi^{\nabla u} \cdot \mathbf{e}_2^c]\!]_2 = \frac{|f_3|}{L_2^{c-}} \tag{9}$$

where $\Phi^{\nabla u}$ is substituted in terms of its projected components $\mathbf{n}^+$ and $\mathbf{t}$ [Fig. 3(c)].

The weak enrichment functions are similarly constructed to satisfy the C^0 continuity condition as

$$\Psi_1^{\nabla u} = \begin{cases} -s_1^+ N_1 & f < 0 \\ -s_1^- N_4 & f > 0 \end{cases} \tag{10a}$$

$$\Psi_2^{\nabla u} = \begin{cases} -s_2^+ N_2 & f < 0 \\ -s_2^- N_3 & f > 0 \end{cases} \tag{10b}$$

These enrichment functions are shown in Figs. 4(c and d). The side-splitter theorem was used in Eq. (10*b*) to further simplify the following terms:

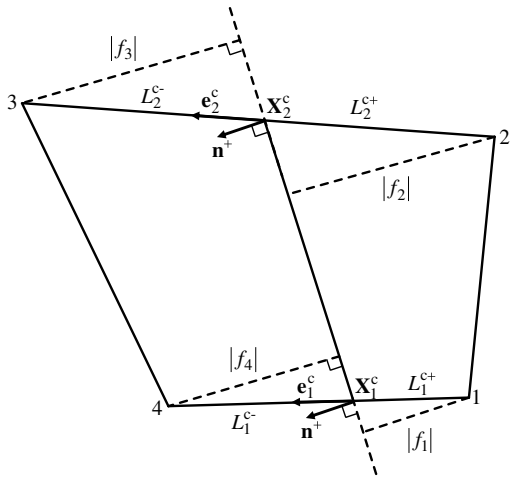

Fig. 5. Nomenclature for a quadrilateral element with a crack passing through nonadjacent sides.

$$\frac{|f_1|}{|f_4|} = \frac{L_1^{c+}}{L_1^{c-}} \quad \text{and} \quad \frac{|f_2|}{|f_3|} = \frac{L_2^{c+}}{L_2^{c-}} \tag{11}$$

In addition, we used the normalized parameters $s_I^- = L_I^{c-}/L_I^c$ and $s_I^+ = L_I^{c+}/L_I^c$.

Enrichment Functions for Crack Passing through Adjacent Edges

Consider a finite element with local node numbers as shown in Fig. 6(a), where a crack has advanced straight from the element edges S_4 to S_1, which are two adjacent edges. In this case, the finite element is partitioned into triangular and pentagonal subdomains. Following the same steps as in the previous section to construct the enrichment functions for the discontinuity Φ^u which is shown in Fig. 6(b), Eq. (3) gives

$$N_2 + N_3 + N_4 = \Psi_1^{u+} + \Psi_2^{u+} \tag{12a}$$

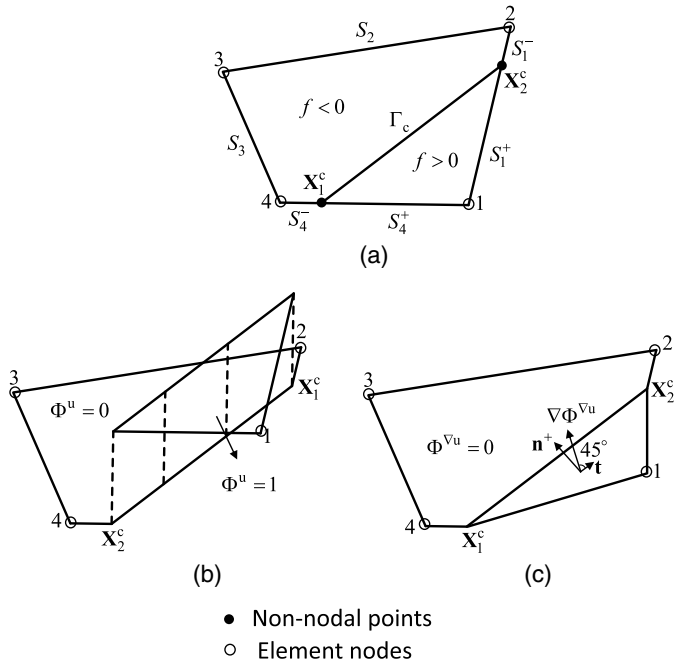

Fig. 6. Representation of a crack for the case when the crack passes through adjacent edges: (a) a two-dimensional quadrilateral element with a crack; (b) Φ^u; and (c) $\Phi^{\nabla u}$.

$$-N_1 = \Psi_1^{u-} + \Psi_2^{u-} \tag{12b}$$

The enrichment functions are constructed so that the C^0 continuity condition is satisfied. In doing so, for the triangular subdomain in Eq. (12*a*), Ψ_1^{u+} and Ψ_2^{u+} must vanish along edges S_1^+ and S_4^+, respectively. For the pentagonal subdomain in Eq. (12*b*), the enrichment functions Ψ_1^{u-} and Ψ_2^{u-} also must vanish along three edges each, i.e., Ψ_1^{u-} along edges S_1^-, S_2, and S_3 and Ψ_2^{u-} along edges S_4^-, S_3, and S_2.

Therefore, to satisfy all these conditions, the enrichment functions are defined as follows

$$\Psi_1^u = \begin{cases} -\dfrac{N_1 N_4}{N_2+N_4} & f<0 \\ N_4 + \dfrac{N_3}{2} & f>0 \end{cases} \quad \text{and}$$

$$\Psi_2^u = \begin{cases} -\dfrac{N_1 N_2}{N_2+N_4} & f<0 \\ N_2 + \dfrac{N_3}{2} & f>0 \end{cases} \tag{13}$$

These enrichment functions are plotted in Figs. 7(a and b). For the triangular subdomain in which $f>0$, because the shape function N_3 vanishes along all the required edges, half of the term N_3 was assigned to each enrichment function. In addition, for the pentagonal subdomain in which $f<0$, the enrichment functions were obtained identical to those of triangular elements proposed by Asareh et al. (2018b).

Finally, for the representation of discontinuity in the derivative of solution fields across the crack interface, i.e., $\Phi^{\nabla u}$ in Fig. 6(c), Eq. (3) gives

$$\begin{aligned} &-N_2|f_2| - N_3|f_3| - N_4|f_4| \\ &\quad = \Psi_1^{\nabla u+}[\![L_1^c \nabla\Phi^{\nabla u}\cdot\mathbf{e}_1^c]\!]_1 + \Psi_2^{\nabla u+}[\![L_2^c \nabla\Phi^{\nabla u}\cdot\mathbf{e}_2^c]\!]_2 \\ &-N_1|f_1| = \Psi_1^{\nabla u-}[\![L_1^c \nabla\Phi^{\nabla u}\cdot\mathbf{e}_1^c]\!]_1 + \Psi_2^{\nabla u-}[\![L_2^c \nabla\Phi^{\nabla u}\cdot\mathbf{e}_2^c]\!]_2 \end{aligned} \tag{14}$$

The dot products in Eq. (14) can be also further replaced with the geometric properties by (Fig. 8)

$$[\![\nabla\Phi^{\nabla u}\cdot\mathbf{e}_1^c]\!]_1 = \frac{|f_4|}{L_1^{c-}} \quad \text{and} \quad [\![\nabla\Phi^{\nabla u}\cdot\mathbf{e}_2^c]\!]_2 = \frac{|f_2|}{L_2^{c-}} \tag{15}$$

Similarly, the weak enrichment functions are constructed so that the C^0 continuity conditions are satisfied for a crack passing through nonadjacent edges as

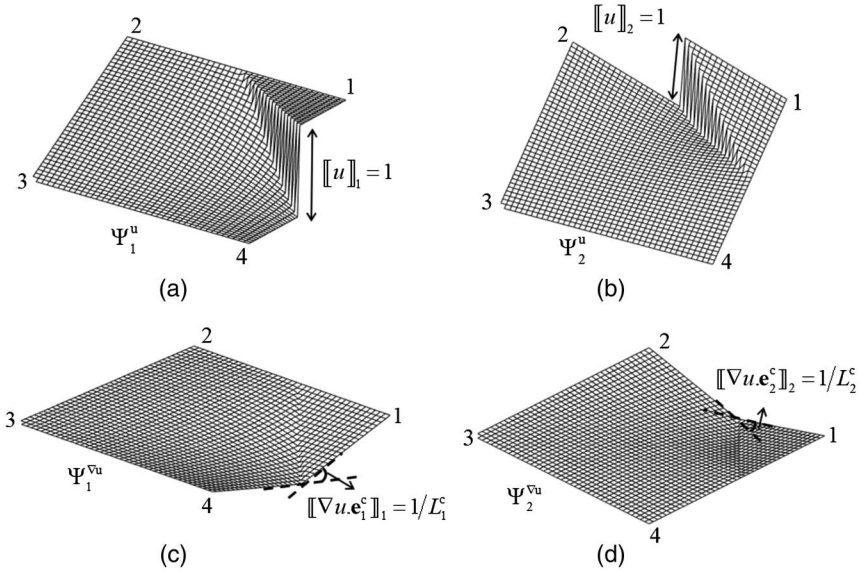

Fig. 7. Enrichment functions for the case when the crack passes through adjacent edges: (a) Ψ_1^u; (b) Ψ_2^u; (c) $\Psi_1^{\nabla u}$; and (d) $\Psi_2^{\nabla u}$.

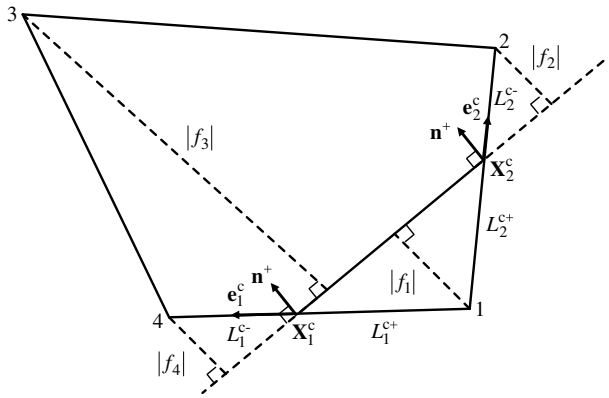

Fig. 8. Nomenclature for a rectangular element with a crack passing through adjacent sides.

$$\Psi_1^{\nabla u} = \begin{cases} -s_1^+ \dfrac{N_1 N_4}{N_2 + N_4} & f < 0 \\ -s_1^- \left(N_4 + \dfrac{|f_3|}{2|f_4|} \right) & f > 0 \end{cases} \quad \text{and}$$

$$\Psi_2^{\nabla u} = \begin{cases} -s_2^+ \dfrac{N_1 N_2}{N_2 + N_4} & f < 0 \\ -s_2^- \left(N_2 + \dfrac{|f_3|}{2|f_2|} \right) & f > 0 \end{cases} \tag{16}$$

These enrichment functions are shown in Figs. 7(c and d). The enrichment functions described in this section were obtained for a particular crack location inside the element. In the next section, the enrichment functions are described for the generalized node numbering permutations.

Generalized Notation for Enrichment Functions

To facilitate implementation of the NXFEM into a general-purpose finite-element library, a generalized notation is further described. To express enrichment functions for an arbitrary finite element which is cut by a crack at two arbitrary finite-element edges, the local node numbers in Fig. 9 can be mapped into actual local node numbers with a proper permutation. The finite-element edges containing the nonnodal points $\mathbf{X}_I^c$ are denoted S_I^c and the element nodes connected to this edge are denoted by $I_I^{c\pm}$ (Fig. 9). Using these notations, Eqs. (7) and (13) can be generalized as

$$\Psi_J^{u\pm} = \begin{cases} \pm N_{I_J^{c\mp}} & \text{for a quadrilateal subdomain} \\ \pm \left(N_{I_J^{c\mp}} + \dfrac{N_{I^{nc}}}{2} \right) & \text{for a triangular subdomain} \\ \pm \dfrac{N_{I_J^{c+}} N_{I_J^{c-}}}{N_{I_1^{c\pm}} + N_{I_2^{c\pm}}} & \text{for a pentagonal subdomain} \end{cases} \tag{17}$$

The sign $\pm$ in the left-hand side may be reversed to $\mp$ in the right-hand side. For the nonadjacent edge crack, the node at the intersection of the edges which are not cut by the crack is denoted by I^{nc}. To compute the enrichment function Ψ^u at a point based on Eq. (17), first, the type of the subdomain where the point resides on is determined, then the sign is selected to be equal to the sign of level set function for the subdomain. Similarly, Eqs. (10) and (16) can also be generalized as

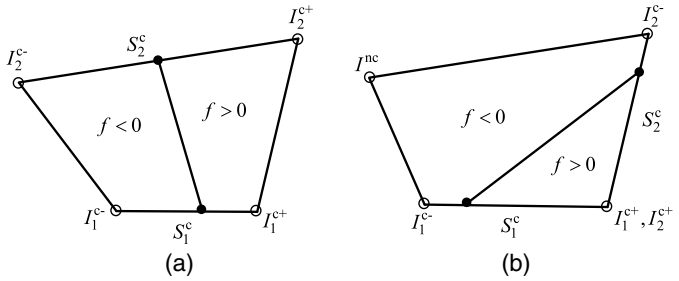

Fig. 9. Generalized node numbering notation for the case in which the crack passes through (a) nonadjacent edges; and (b) adjacent edges.

$$\Psi_J^{\nabla u\pm} = \begin{cases} -s_J^{\mp} N_{I_J^{c\mp}} & \text{for a quadrilateal subdomain} \\ -s_J^{\mp} \left(N_{I_J^{c\mp}} + \dfrac{N_{I^{nc}} |f_{I^{nc}}|}{2|f_{I_J^{c\mp}}|} \right) & \text{for a triangular subdomain} \\ -s_J^{\mp} \dfrac{N_{I_J^{c+}} N_{I_J^{c-}}}{N_{I_1^{c\pm}} + N_{I_2^{c\pm}}} & \text{for a pentagonal subdomain} \end{cases} \tag{18}$$

Such a unified notation can be also used for three-node triangular elements (Appendix).

Weak Form and Discretized Equations

The linear momentum equation in a total Lagrangian description is given by

$$\frac{\partial \mathbf{P}_{ji}}{\partial X_j} + \rho \mathbf{b}_i - \rho \ddot{u}_i = 0 \text{ in } \Omega \tag{19}$$

where $\mathbf{P}$ = nominal stress tensor; ρ = initial density; and $\mathbf{b}$ is the body force vector per unit mass. The boundary conditions can be written

$$\begin{aligned} u_i &= \bar{u}_i \text{ on } \Gamma_u \\ [\![u]\!]_i &= [\![\bar{u}]\!]_i \text{ on } \Gamma_{uc} \\ [\![\nabla u]\!]_i &= [\![\nabla \bar{u}]\!]_i \text{ on } \Gamma_{\nabla uc} \\ n_j P_{ji} &= \bar{t}_i \text{ on } \Gamma_t \\ n_j^{\pm} P_{ji}^{\pm} &= \tau_i^c([\![u]\!]_i) \text{ on } \Gamma_c \end{aligned} \tag{20}$$

where $\bar{\mathbf{u}}$ = prescribed displacement on the Dirichlet boundary Γ_u; $[\![\bar{\mathbf{u}}]\!]$ and $[\![\nabla \bar{\mathbf{u}}]\!]$ = prescribed jumps in the displacement and its gradient on sets of nonnodal points located on Γ_{uc} and $\Gamma_{\nabla uc}$, respectively; τ^c = pseudotraction distributed on the crack surface; and $\bar{\mathbf{t}}$ = prescribed traction on the Neumann boundary Γ_t. In this study, we adopt an elementwise crack propagation scheme. Thus, the crack tip modeling requires imposing homogeneous prescribed displacement jumps as

$$[\![u]\!]_i = [\![\nabla u]\!]_i = 0 \tag{21}$$

at the crack tip which is located at the finite-element edge.

We define the spaces for the admissible displacement field $\mathbf{u}$ and the test field $\delta \mathbf{u}$ as

$$\mathcal{U} = \{\mathbf{u} \in \mathrm{C}^0 | \mathbf{u} = \bar{\mathbf{u}} \text{ on } \Gamma_u,$$
$$[\![\mathbf{u}]\!] = [\![\bar{\mathbf{u}}]\!] \text{ on } \Gamma_{uc}, \mathbf{u} \text{ discontiniuous on } \Gamma_c\}$$
$$\mathcal{U}_0 = \{\delta\mathbf{u} \in C | \delta\mathbf{u} = 0 \text{ on } \Gamma_u,$$
$$[\![\delta\mathbf{u}]\!] = 0 \text{ on } \Gamma_{uc}, \delta\mathbf{u} \text{ discontiniuous on } \Gamma_c\}$$

The weak form of Eq. (19) can be stated as find $\mathbf{u} \in \mathcal{U}$, for $\delta\mathbf{u} \in \mathcal{U}_0$

$$\int_\Omega \delta\mathbf{u} \cdot \rho\ddot{\mathbf{u}} \mathrm{d}\Omega = \int_\Omega \delta\mathbf{u} \cdot \rho\mathbf{b} \mathrm{d}\Omega + \int_{\Gamma_t} \delta\mathbf{u} \cdot \bar{\mathbf{t}} \mathrm{d}\Gamma_t - \int_\Omega \delta\mathbf{F}^T : \mathbf{P} \mathrm{d}\Omega - \int_{\Gamma_c} [\![\delta\mathbf{u}]\!] \cdot \boldsymbol{\tau}^c \mathrm{d}\Gamma_c \quad (22)$$

where $\mathbf{F}$ = deformation gradient. The weak form, i.e., Eq. (22) is discretized by

$$\int_{\Omega^e} \rho\mathbf{N}^T\mathbf{N} \mathrm{d}\Omega^e \ddot{\mathbf{d}}_e = \int_{\Omega^e} \rho\mathbf{N}^T\mathbf{b} \mathrm{d}\Omega^e + \int_{\Gamma_t^e} \mathbf{N}^T\bar{\mathbf{t}} \mathrm{d}\Gamma_t^e - \int_{\Omega^e} \mathbf{B}^T\mathbf{S} \mathrm{d}\Omega^e - \int_{\Gamma_c^e} [\![\boldsymbol{\Psi}]\!]_e^T \boldsymbol{\tau}^c \mathbf{n} \mathrm{d}\Gamma_c^e \quad (23)$$

where $\mathbf{S}$ = second Piola-Kirchhoff stress in Voigt form; and $\mathbf{d}_e$ = generalized nodal coefficient matrix including the nodal displacements and the enrichment parameters. It can be expanded for a four-node quadrilateral element as

$$\mathbf{d}_e = [\mathbf{u}_1, \mathbf{u}_2, \mathbf{u}_3, \mathbf{u}_4, [\![\mathbf{u}]\!]_1, L_1^c [\![\nabla\mathbf{u} \cdot \mathbf{e}_1^c]\!]_1, [\![\mathbf{u}]\!]_2, L_2^c [\![\nabla\mathbf{u} \cdot \mathbf{e}_2^c]\!]_2]^T \quad (24)$$

The generalized shape function vector $\mathbf{N}$ is defined as

$$\mathbf{N} = [\mathbf{N}_1, \mathbf{N}_2, \mathbf{N}_3, \mathbf{N}_4, \boldsymbol{\Psi}_1^u, \boldsymbol{\Psi}_1^{\nabla u}, \boldsymbol{\Psi}_2^u, \boldsymbol{\Psi}_2^{\nabla u}] \quad (25)$$

The shape function derivative matrix associated to the node I is denoted by $\mathbf{B}_I$ and constructed as

$$\mathbf{B}_I = [\mathbf{B}_I^0, \mathbf{B}_I^u, \mathbf{B}_I^{\nabla u}] \quad (26)$$

where

$$\mathbf{B}_I^0 = \begin{bmatrix} N_{I,X}x_{,X} & N_{I,X}y_{,X} \\ N_{I,Y}x_{,Y} & N_{I,Y}y_{,Y} \\ N_{I,X}x_{,Y} + N_{I,Y}x_{,X} & N_{I,X}y_{,Y} + N_{I,Y}y_{,X} \end{bmatrix}$$

$$\mathbf{B}_I^u = \begin{bmatrix} \Psi_{I,X}^u x_{,X} & \Psi_{I,X}^u y_{,X} \\ \Psi_{I,Y}^u x_{,Y} & \Psi_{I,Y}^u y_{,Y} \\ \Psi_{I,X}^u x_{,Y} + \Psi_{I,Y}^u x_{,X} & \Psi_{I,X}^u y_{,Y} + \Psi_{I,Y}^u y_{,X} \end{bmatrix}$$

$$\mathbf{B}_I^{\nabla u} = \begin{bmatrix} \Psi_{I,X}^{\nabla u} x_{,X} & \Psi_{I,X}^{\nabla u} y_{,X} \\ \Psi_{I,Y}^{\nabla u} x_{,Y} & \Psi_{I,Y}^{\nabla u} y_{,Y} \\ \Psi_{I,X}^{\nabla u} x_{,Y} + \Psi_{I,Y}^{\nabla u} x_{,X} & \Psi_{I,X}^{\nabla u} y_{,Y} + \Psi_{I,Y}^{\nabla u} y_{,X} \end{bmatrix}$$

where $(\cdot)_{,i}$ represents the spatial derivative of $(\cdot)$ along the ith coordinate direction.

Time-Stepping Algorithm

The explicit central difference time-stepping algorithm is conditionally stable, i.e., it is stable if

$$\Delta t \le \Delta t_c = \frac{2}{\omega_{\max}} \quad (27)$$

where Δt and Δt_c = simulation and critical time integration step sizes, respectively; and $\omega_{\max}$ = highest frequency of the discrete system. For the assessment of Δt_c, the frequencies ω_i of the one-dimensional discrete system $\omega_i^2 \mathbf{M}\mathbf{d}_i = \mathbf{K}\mathbf{d}_i$ can be investigated with the normalized location of the predetermined crack (Song et al. 2006). However, as was reported by Song et al. (2006), for a consistent mass matrix the critical time size drops linearly to zero as the crack location approaches to the element nodes.

To circumvent such a difficulty, a specific lumped mass matrix with an explicit-implicit time-step algorithm (Belytschko and Mullen 1976, 1978) was adopted with the conventional Newmark-beta method. In previous studies, the explicit-implicit methods were successfully used in XFEM (Belytschko et al. 2003) and meshfree methods (Rabczuk and Belytschko 2007). In the method, the nodal displacements $\mathbf{d}$ and velocities $\mathbf{v}$ are updated at time increment $n+1$ as

$$\mathbf{d}_{n+1} = \tilde{\mathbf{d}}_{n+1} + \beta\Delta t^2 \mathbf{a}_{n+1} \quad (28a)$$

$$\mathbf{v}_{n+1} = \tilde{\mathbf{v}}_{n+1} + \gamma\Delta t \mathbf{a}_{n+1} \quad (28b)$$

where $\mathbf{a}$ = nodal accelerations; and $\tilde{\mathbf{d}}_{n+1}$ and $\tilde{\mathbf{v}}_{n+1}$ pertain to the time step n as

$$\tilde{\mathbf{d}}_{n+1} = \mathbf{d}_n + \Delta t \mathbf{v}_n + \frac{\Delta t^2}{2}(1-2\beta)\mathbf{a}_n \quad (29a)$$

$$\tilde{\mathbf{v}}_{n+1} = \mathbf{v}_n + (1-\gamma)\Delta t \mathbf{a}_n \quad (29b)$$

In the proposed time-stepping algorithm, the total degrees of freedom are partitioned into explicit $\{E\}$ and implicit $\{I\}$ sets; the regular degrees of freedom are treated explicitly with Newmark-beta parameters $\beta = 0$ and $\gamma = 1/2$, whereas the enriched degrees of freedom are treated implicitly with Newmark-beta parameters $\beta = 1/4$ and $\gamma = 1/2$. The mathematical analysis of the stability of the adopted explicit-implicit time integration scheme will be described in the authors' future work.

Cohesive Law

A linear cohesive model is used for the damage evolution created by the crack. The cohesive traction is computed using a radial-return algorithm by Asareh et al. (2018b). Mode 1 is considered the dominant failure mode of the subsequently described failure problems. Therefore, only the normal component of the cohesive traction is defined in terms of the normal displacement jump δ_N as

$$\delta_N = \mathbf{n} \cdot [\![\mathbf{u}]\!] = \mathbf{n} \cdot \sum_{J \in \delta_{\mathrm{NP}}^K} ([\![\boldsymbol{\Psi}_J^u]\!] [\![\mathbf{u}]\!]_J + [\![\boldsymbol{\Psi}_J^{\nabla u}]\!] [\![L_J^c \nabla\mathbf{u} \cdot \mathbf{e}_J^c]\!]_J) \quad (30)$$

The proposed weak enrichment functions $\Psi^{\nabla u}$ are not in general continuous across the interface. Therefore they contribute to cohesive force computations.

Numerical Examples

In this section, the performance of the NXFEM with four-node quadrilateral elements is demonstrated with three numerical examples. In the first example, the convergence study of the proposed method is performed with static near-tip field problems. The relative errors in the energy- and L^2-norms are denoted $\mathrm{RE}_{\mathrm{en}}$ and RE_d, respectively, and defined as

$$(\mathrm{RE}_{\mathrm{en}})^2 = \frac{\int_\Omega (\boldsymbol{\varepsilon} - \boldsymbol{\varepsilon}^h)^T \mathbf{C} (\boldsymbol{\varepsilon} - \boldsymbol{\varepsilon}^h) \mathrm{d}\Omega}{\int_\Omega \boldsymbol{\varepsilon}^T \mathbf{C} \boldsymbol{\varepsilon} \mathrm{d}\Omega},$$
$$(\mathrm{RE}_d)^2 = \frac{\int_\Omega (\mathbf{u} - \mathbf{u}^h)^2 \mathrm{d}\Omega}{\int_\Omega \mathbf{u}^2 \mathrm{d}\Omega} \tag{31}$$

In this analysis, linear elastic fracture mechanics is adopted, and the results are compared with the convergence rates of the conventional XFEM and the NXFEM with three-node triangular elements which are previously reported by Asareh et al. (2018a); in the subsequent figures for the convergence study, log denotes $\log_{10}$.

In addition, the last two numerical examples demonstrate the performance of the NXFEM for dynamic failure. In these examples, an explicit-implicit time integration scheme with Courant number of 0.8 is used. Because the enriched degrees of freedom are treated implicitly, the crack can be placed close to the finite-element nodes. Plane strain condition with the unit thicknesses is considered. A crack is initiated in a finite element when the maximum principle stress reaches to the tensile strength of $\tau_{\max}$. After the crack initiation, linear cohesive forces dissipate the fracture energy of G_F until the crack opening reaches the critical crack opening displacement $\delta_{\max}$. The fracture criterion used in this study is the maximum tensile stress computed at the crack edge. The direction of the crack is selected to be normal to the maximum tensile stress direction. Details about the adopted cohesive crack model and fracture criterion were given by Asareh et al. (2018b).

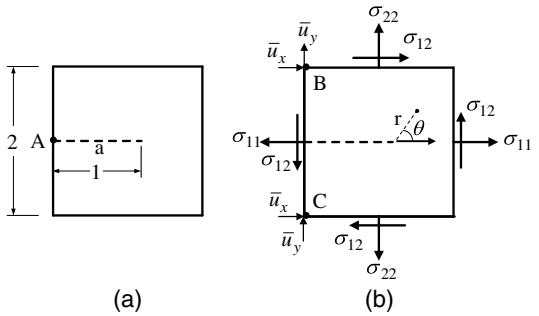

Fig. 10. Square patch for the near-tip crack problem: (a) geometry; and (b) boundary conditions.

Convergence Study of NXFEM with Near-Tip Fields

To verify the linear completeness of the proposed enrichment functions for quadrilateral elements, a convergence study was performed on near-tip crack field problem. A biunit square patch with side length $L = 2$ and an initial crack length $a = 1$ was considered (Fig. 10). The Young's modulus was $E = 1.0 \times 10^5$ and the Poisson's ratio was $\nu = 0.3$. The stress intensity factor was prescribed as $K_I = 1.0$.

Convergence studies for energy- and L^2-norms were performed using uniform four-node quadrilateral $L_h \times L_h$ meshes, where $L_h = 10$, 20, 40, and 80. The elements were structured so that the initial crack passed through the middle points of nonadjacent edges. The convergence study was performed for three different approaches (Fig. 11): (1) the standard XFEM, (2) the NXFEM adopting only strong enrichment functions Ψ^u as in Asareh et al. (2018b), and (3) the linear complete NXFEM as in Asareh et al. (2018a). In Fig. 11, the standard XFEM and the linear complete NXFEM had identical results when the crack propagates aligned the center of the four-node quadrilateral elements through the nonadjacent edges, and thus only one curve is shown. The convergence study suggests that the rates of convergence in the energy norm for the standard XFEM and linear complete NXFEM are close to the optimal convergence rate, i.e., 0.5 (Babuška and Melenk 1997; Asareh et al. 2018a). The results also show that the NXFEM with only Ψ^u enrichment underperforms the other methods, but its convergence rate improves with mesh refinement [Fig. 11(b)].

The convergence rates of the linear complete NXFEM for four-node quadrilateral elements were compared with the convergence rates of triangular elements reported by Asareh et al. (2018a). Relatively lower errors were observed for quadrilateral elements (Fig. 12). In addition, the convergence rates were slightly higher than those obtained with triangular elements.

To improve the accuracy of the NXFEM, a closed-form solution for the displacement jumps can be imposed at the nonnodal Point A in Fig. 10(a); in the NXFEM, the kinematic constrains on the crack interface can be treated as Dirichlet boundary conditions. The convergence results in L^2-norm are shown in Fig. 13. For the case of the NXFEM only with a strong discontinuity enrichment function, the error made a constant shift toward lower error with small improvement in the convergence rate. However, for the linear complete NXFEM case, both relative errors and convergence rates improved.

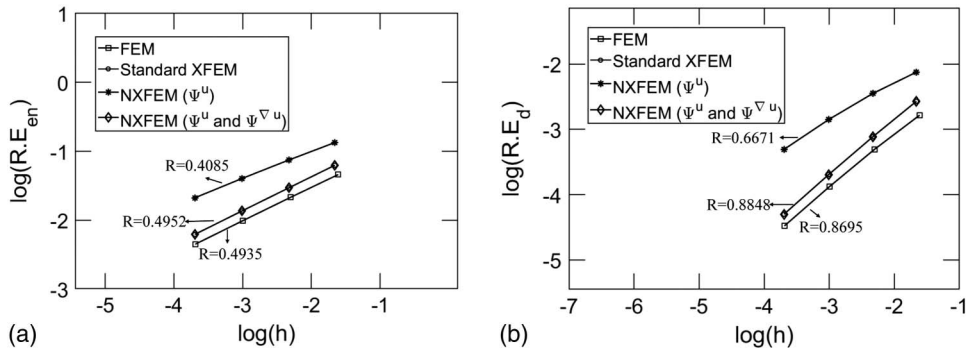

Fig. 11. Convergence study for the near-tip crack problem: (a) energy-norm errors; and (b) L^2-norm errors.

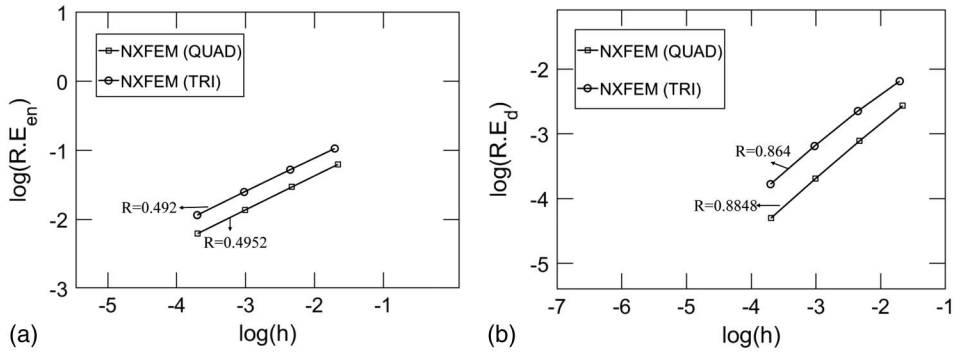

Fig. 12. Comparison of the convergence rates of the linear complete NXFEM between four-node quadrilateral elements and three-node triangular elements (Asareh et al. 2018a): (a) energy-norm errors; and (b) L^2-norm errors.

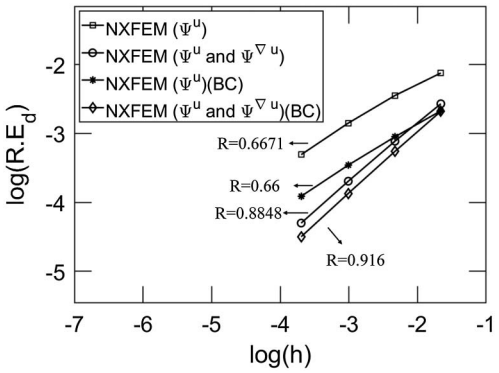

Fig. 13. Rates of convergence in L^2-norm errors of the near-tip crack problem for the NXFEM with and without Dirichlet boundary conditions on the interface.

Edge-Cracked Plate under Impulsive Loading

Kalthoff and Winkler (1988) conducted a series of experiments on an edge-cracked plate impacted by a projectile [Fig. 14(a)]. At lower impact velocities, a brittle fracture with a crack propagation at angle of about 70° with respect to initial notch was observed. This example was selected to further examine the capabilities of the nonnodal quadrilateral elements for modeling dynamic crack propagation, compared with triangular elements in Asareh et al. (2018a).

Due to twofold symmetry, the upper half of the plate was modeled with the symmetry condition $u_y = 0$ imposed at its bottom edge [Fig. 14(b)]. Considering identical elastic impedance for the plate and the projectile, half of the applied velocity, i.e., 16.5 m/s was imposed as a step function on the left edge on $0 \le y \le 25$ mm.

The material parameters were $\rho = 8{,}000$ kg/m^3, $E = 190$ GPa, and $\nu = 0.3$; for such material properties, the Rayleigh wave speed was about $C_R = 2{,}800$ m/s. Tensile strength of $\tau_{\max} = 844$ MPa and fracture energy of $G_F = 2.213 \times 10^4$ N/m were used. To examine the mesh sensitivity of the NXFEM, the model was discretized with two different uniform meshes: 40×40 and 80×80 meshes. In Fig. 15, the crack paths are shown for the 80×80 mesh.

Similar results were observed for the 40×40 mesh; the trajectories of crack growth for both meshes are compared in Fig. 16. Both simulations yielded similar crack paths. The crack propagation angles and timing data are listed in Table 1. The data show that the crack began to propagate at earlier times with mesh refinement which agrees well with those obtained by Asareh et al. (2018a).

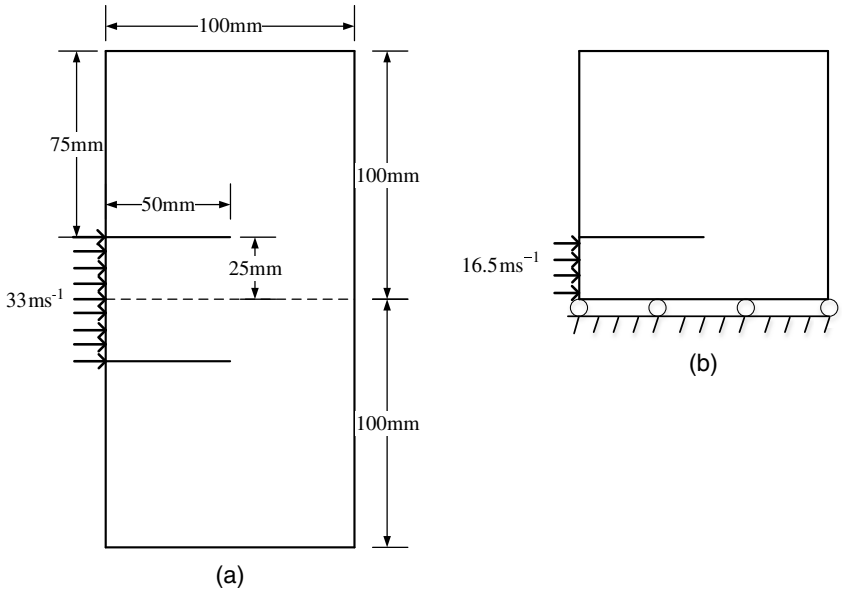

Fig. 14. (a) Kalthoff experimental setup; and (b) upper half of the plate analyzed due to twofold symmetry. (Modified from Asareh et al. 2018a.)

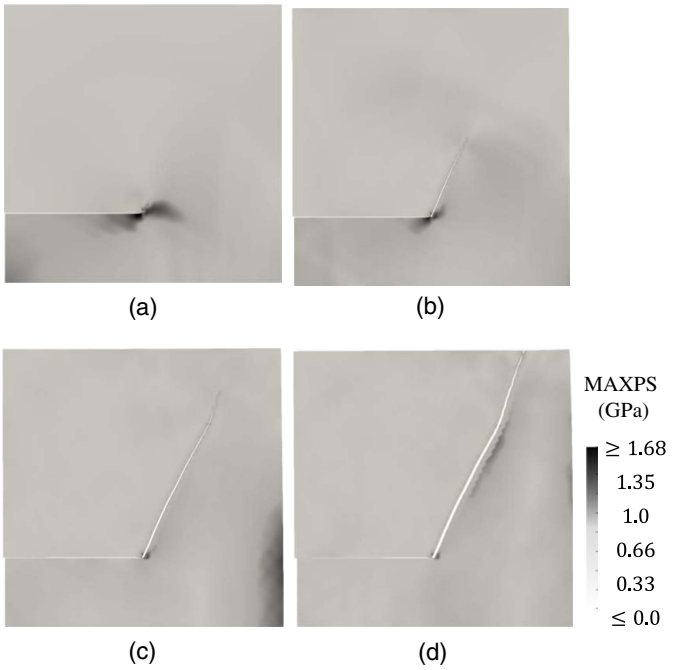

Fig. 15. Computed crack paths using nonnodal quadrilateral elements on the 80 × 80 deformed mesh with a maximum principle stress at different time steps: (a) $t = 26.7$ μs; (b) $t = 39.66$ μs; (c) $t = 58.45$ μs; and (d) $t = 89.0$ μs. (Modified from Asareh et al. 2018a.)

The crack first propagated nearly straight along an initial angle until around $t = 55$ μs; then, after a minor spurt upward, it continued to grow primarily along the initial angle. For both meshes, the initial and overall crack propagation angles were around 60°, which compares well with the observed value of 70°. However, these crack propagation angles were slightly lower than the angles reported by Asareh et al. (2018b). This discrepancy may be attributed to the explicit-implicit time integration used in the present study with Courant number of 0.8.

Comparisons of the crack tip propagation speeds between triangular elements and quadrilateral elements with the NXFEM are shown in Fig. 17; the results for the NXFEM with triangular element were taken from Asareh et al. (2018a). It is clear that the crack speeds of quadrilateral elements had less mesh sensitivity compared with the crack propagation speeds of triangular elements with the NXFEM. In addition, for quadrilateral elements, the crack propagation speed rarely exceeded 2,000 m/s, which is about 70% of the Raleigh wave speed. For both methods, from the beginning until 60 μs, the crack propagation speed was lower for the coarse mesh than for the fine mesh. However, near the termination of the simulation, the computed crack speed decelerated more rapidly for the fine mesh than for the coarse mesh. Nevertheless, the crack speed for the NXFEM had less mesh dependency than those obtained using the conventional XFEM (Belytschko et al. 2003; Asareh et al. 2018a).

Table 1. Crack propagation angles and timing data using nonnodal quadrilateral elements for Kalthoff's experiment

	Angles (degrees)		Time (μs)	
Mesh	Initial	Overall	Propagation	Simulation
40 × 40	57.93	58.44	26.72	88.25
80 × 80	59.47	59.93	24.28	81.96

Compact Compression Specimen Test

In the numerical example, a mixed-mode dynamic crack propagation in a brittle material, i.e., polymethylmethacrylate (PMMA), was investigated with the compact compression specimen (CCS) experiments (Rittel and Maigre 1996; Rittel et al. 1996). Various numerical methods have been applied to predict this mixed-mode failure problem (Paulino et al. 2010; Leon et al. 2014; Menouillard et al. 2006). The geometry of the specimen and the prescribed boundary conditions are shown in Fig. 18(a).

The applied impact load by a projectile was modeled with a ramp velocity function as

$$V(t) = \begin{cases} V_0 t/t_{\text{ramp}} & t < t_{\text{ramp}} \\ V_0 & t \geq t_{\text{ramp}} \end{cases} \tag{32}$$

where $V_0 = 20$ m/s and $t_{\text{ramp}} = 40$ μs. The material properties of PMMA are density $\rho = 1{,}180$ kg/m^3, Young's modulus $E = 5.76$ GPa, and Poisson's ratio $\nu = 0.42$. Across the discontinuity, i.e., crack, a linear cohesive model was imposed; the cohesive input

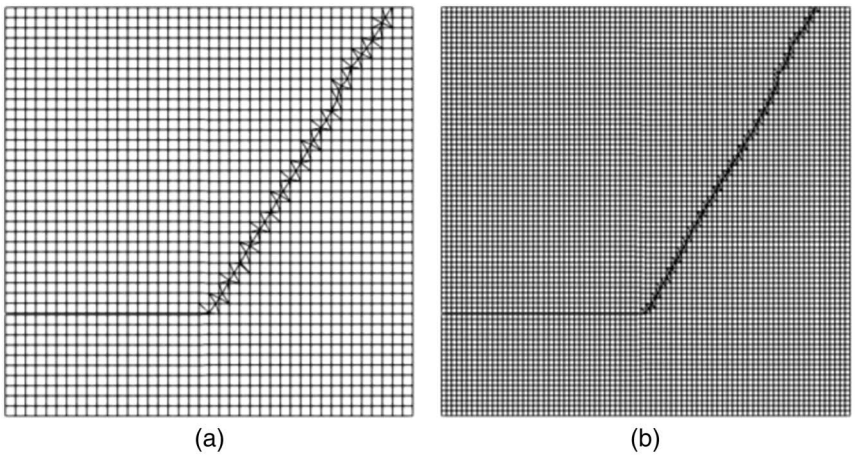

Fig. 16. Crack propagation trajectories at final simulation step using nonnodal quadrilateral elements: (a) 40 × 40 mesh; and (b) 80 × 80 mesh. (Modified from Asareh et al. 2018a.)

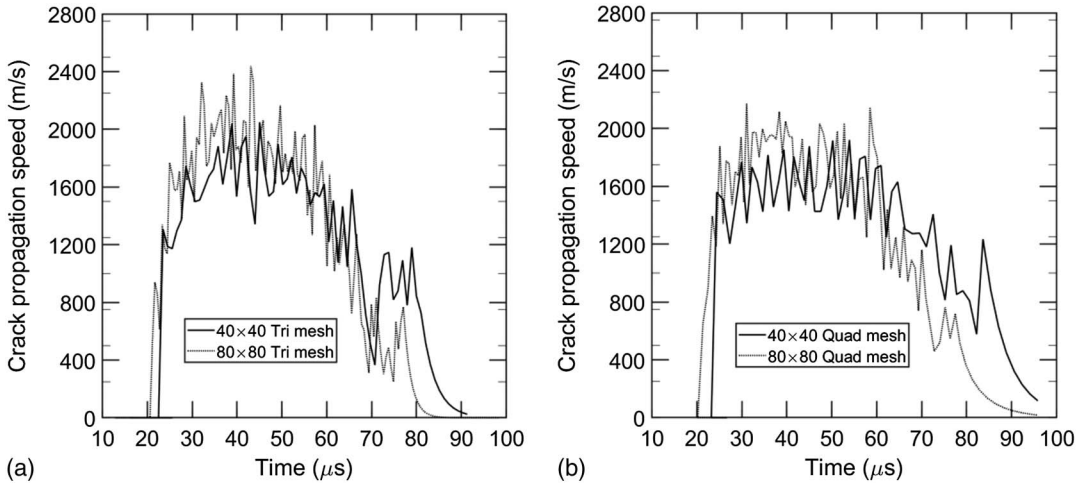

Fig. 17. Computed crack propagation speeds for Kolthoff's experiment: a linear complete NXFEM with (a) three-node triangular elements; and (b) four-node quadrilateral elements. (Modified from Asareh et al. 2018a.)

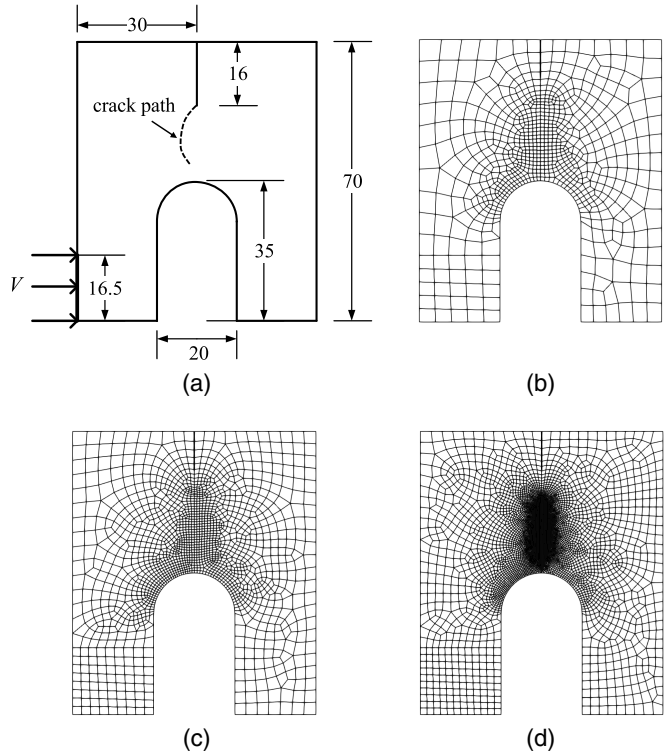

Fig. 18. Geometry and boundary conditions of compact compression specimen test and finite-element meshes with approximate average element size h^{avg} in the middle part of the model: (a) experimental setup; (b) coarse mesh ($h^{avg} = 1$ mm); (c) medium mesh ($h^{avg} = 0.65$ mm); and (d) fine mesh ($h^{avg} = 0.25$ mm). All dimensions are in millimeters.

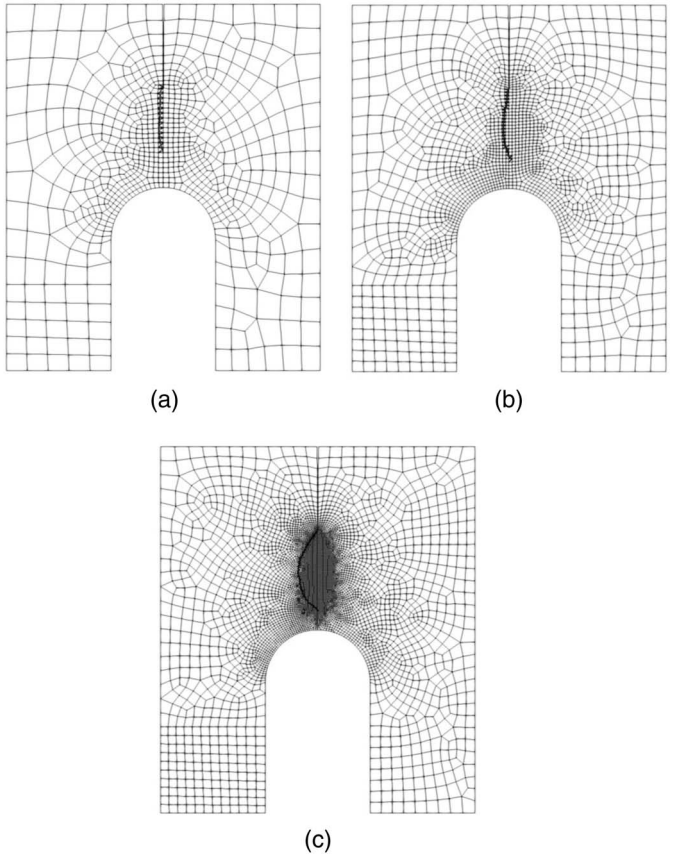

Fig. 19. Crack propagation trajectories at time around $t = 130$ μs: (a) coarse mesh; (b) medium mesh; and (c) fine mesh.

parameters were fracture energy $G_F = 352.3$ Jm^{-2} and cohesive strength $\sigma_{max} = 129.6$ MPa.

To test the mesh sensitivity of the NXFEM, numerical simulations were carried out with three different irregular meshes [Figs. 18(b–d)]. For comparisons, the simulations were performed with both the conventional XFEM and the linear complete NXFEM; i.e., six simulations in total. The crack paths obtained with the NXFEM are shown in Fig. 19. Similar crack paths were found for the standard XFEM. However, the experimentally observed crack path was only captured by the fine mesh, whereby the initial crack angle of 54.11° with the horizontal axis was obtained, which is similar to the experimental observation of about 45°. This mesh dependency may be due to the fact that the coarse mesh cannot properly capture the complicated stress status as the crack tip

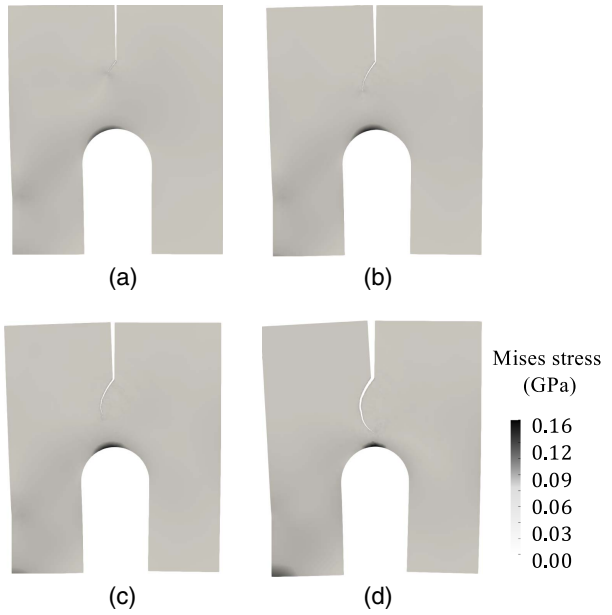

Fig. 20. Computed crack paths of the fine mesh on deformed configuration with a von Mises stress at different time steps: (a) $t = 76.8$ μs; (b) $t = 93.77$ μs; (c) $t = 102.79$ μs; and (d) $t = 130.92$ μs.

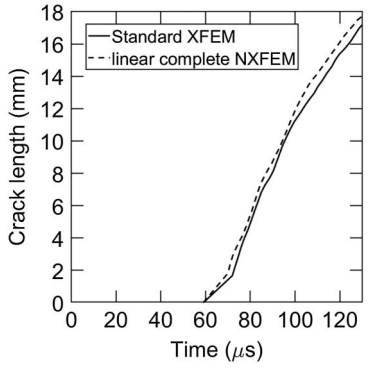

Fig. 21. Time history of crack length for the fine mesh.

propagates near the curved boundary; the evolution of von Mises stress and the trajectory of crack path are shown in Fig. 20 for the fine mesh, i.e., $h^{\text{avg}} = 0.25$ mm. The crack began to propagate at around 62 μs along the initial angle until $t = 76$ μs. Then the crack changed direction toward the center of the specimen.

Fig. 21 shows the time history of crack length for the fine mesh; the NXFEM result is compared with the conventional XFEM. The two methods gave similar results, which compare well with the computation by Menouillard et al. (2006).

Conclusions

A linear complete nonnodal extended finite-element method (NXFEM) was further developed for modeling crack with four-node quadrilateral elements. In this approach, the enrichment functions are defined so that they satisfy the linear completeness of the enriched finite element, which is the key idea of the NXFEM (Asareh et al. 2018b). Formalism for the enrichment functions was developed for two generic cases: (1) when the crack passes through nonadjacent finite-element edges of a quadrilateral element, and (2) when the crack intersects the adjacent edges. In the NXFEM approach, the discontinuities in a function and its derivative are captured by enriching a set of nonnodal points on the discontinuity interface, in contrast to enriching element nodes in the standard XFEM. In this approach, the physically based enrichment parameters associated with each discontinuity are assigned to nonnodal points; this distinct feature of the NXFEM also facilitates the implementation of this method to pre-existing finite-element analysis programs. The enrichment functions, in turn, are constructed so that they not only vanish outside the element domain but they also reproduce can two independent linear functions on each side of the crack.

The validity of the proposed method was examined through a set of convergence studies of the near-tip field problem in linear elastic fracture mechanics. In these simulations, because the mesh was constructed so that the crack passed through the middle of nonadjacent finite-element edges, the NXFEM had an identical convergence rate as the standard XFEM. However, by imposing Dirichlet constraints on the crack interface, which is one of the advantages of the NXFEM, the convergence rates can be further improved.

The effectiveness of the method for dynamic failure was demonstrated with two numerical examples for which experimental results are available. For Kalthoff's experiment, the proposed method had less mesh dependency than the standard XFEM. However, for the compact compression test, only the fine mesh reproduced the crack pattern observed in the experiment. Moreover, the numerical results suggested that finer mesh is required to match the crack initial propagation angle with those of experiments. This is mainly due to the complicated stress status emanating from mixed-model failure.

Using the NXFEM to capture the discontinuities in both a function and its derivative can facilitate predicting failure in many engineering fracture problems, including dynamic failure along a bimaterial interface. This effort is currently being undertaken by the authors.

Appendix: General Formulation for Three-Node Triangular Elements

The nonnodal enrichment functions for the NXFEM with three-node triangular elements were introduced by Asareh et al. (2018a, b) and can be defined by the same generalized notations used in the present study. In doing so, the strong enrichment functions for three-node triangular element in Fig. 22 can be constructed by

$$\Psi_J^{u\pm} = \begin{cases} \pm N_{I_J^{c\mp}} & \text{for a triangular subdomain} \\ \pm \dfrac{N_{I_J^{c+}} N_{I_J^{c-}}}{N_{I_1^{c\pm}} + N_{I_2^{c\pm}}} & \text{for a quadrilateal subdomain} \end{cases} \tag{33}$$

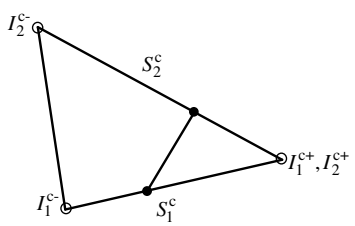

Fig. 22. Illustration of the generalized notation for three-node triangular element.

whereas the weak enrichment functions for triangular element are described by

$$\Psi_J^{\nabla u\pm} = \begin{cases} -s_J^{\mp} N_{I_J^{c\mp}} & \text{for a triangular subdomain} \\ -s_J^{\mp} \dfrac{N_{I_J^{c+}} N_{I_J^{c-}}}{N_{I_1^{c\pm}} + N_{I_2^{c\pm}}} & \text{for a rectangular subdomain} \end{cases} \tag{34}$$

A straight crack subdivides a triangular element into triangular and quadrilateal subdomains.

References

Adalsteinsson, D., and J. A. Sethian. 1995. "A fast level set method for propagating interfaces." *J. Comput. Phys.* 118 (2): 269–277. https://doi.org/10.1006/jcph.1995.1098.

Aragón, A. M., and A. Simone. 2017. "The discontinuity-enriched finite element method." *Int. J. Numer. Methods Eng.* 112 (11): 1589–1613. https://doi.org/10.1002/nme.5570.

Areias, P., M. Msekh, and T. Rabczuk. 2016. "Damage and fracture algorithm using the screened Poisson equation and local remeshing." *Eng. Fract. Mech.* 158 (Jun): 116–143. https://doi.org/10.1016/j.engfracmech.2015.10.042.

Areias, P., and T. Rabczuk. 2017. "Steiner-point free edge cutting of tetrahedral meshes with applications in fracture." *Finite Elem. Anal. Des.* 132 (Sep): 27–41. https://doi.org/10.1016/j.finel.2017.05.001.

Areias, P., T. Rabczuk, and D. Dias-da Costa. 2013. "Element-wise fracture algorithm based on rotation of edges." *Eng. Fract. Mech.* 110 (Sep): 113–137. https://doi.org/10.1016/j.engfracmech.2013.06.006.

Areias, P., J. Reinoso, P. Camanho, J. C. de Sá, and T. Rabczuk. 2018. "Effective 2D and 3D crack propagation with local mesh refinement and the screened Poisson equation." *Eng. Fract. Mech.* 189 (Feb): 339–360. https://doi.org/10.1016/j.engfracmech.2017.11.017.

Asareh, I., T.-Y. Kim, and J.-H. Song. 2018a. "A linear complete extended finite element method for dynamic fracture simulation with non-nodal enrichments." *Finite Elem. Anal. Des.* 152 (Nov): 27–45. https://doi.org/10.1016/j.finel.2018.09.002.

Asareh, I., Y.-C. Yoon, and J.-H. Song. 2018b. "A numerical method for dynamic fracture using the extended finite element method with non-nodal enrichment parameters." *Int. J. Impact Eng.* 121 (Nov): 63–76. https://doi.org/10.1016/j.ijimpeng.2018.06.012.

Babuška, I., and J. M. Melenk. 1997. "The partition of unity method." *Int. J. Numer. Methods Eng.* 40 (4): 727–758. https://doi.org/10.1002/(SICI)1097-0207(19970228)40:4<727::AID-NME86>3.0.CO;2-N.

Belytschko, T., and T. Black. 1999. "Elastic crack growth in finite elements with minimal remeshing." *Int. J. Numer. Methods Eng.* 45 (5): 601–620. https://doi.org/10.1002/(SICI)1097-0207(19990620)45:5<601::AID-NME598>3.0.CO;2-S.

Belytschko, T., H. Chen, J. Xu, and G. Zi. 2003. "Dynamic crack propagation based on loss of hyperbolicity and a new discontinuous enrichment." *Int. J. Numer. Methods Eng.* 58 (12): 1873–1905. https://doi.org/10.1002/nme.941.

Belytschko, T., N. Moës, S. Usui, and C. Parimi. 2001. "Arbitrary discontinuities in finite elements." *Int. J. Numer. Methods Eng.* 50 (4): 993–1013. https://doi.org/10.1002/1097-0207(20010210)50:4<993::AID-NME164>3.0.CO;2-M.

Belytschko, T., and R. Mullen. 1976. "Mesh partitions of explicit-implicit time integration." In *Formulations and computational algorithms in finite element analysis*, 673–690. Cambridge, MA: MIT Press.

Belytschko, T., and R. Mullen. 1978. "Stability of explicit-implicit mesh partitions in time integration." *Int. J. Numer. Methods Eng.* 12 (10): 1575–1586. https://doi.org/10.1002/nme.1620121008.

Bordas, S., T. Rabczuk, and G. Zi. 2008. "Three-dimensional crack initiation, propagation, branching and junction in non-linear materials by an extended meshfree method without asymptotic enrichment." *Eng. Fract. Mech.* 75 (5): 943–960. https://doi.org/10.1016/j.engfracmech.2007.05.010.

Chau-Dinh, T., G. Zi, P.-S. Lee, T. Rabczuk, and J.-H. Song. 2012. "Phantom-node method for shell models with arbitrary cracks." *Comput. Struct.* 92 (Feb): 242–256. https://doi.org/10.1016/j.compstruc.2011.10.021.

Chessa, J., H. Wang, and T. Belytschko. 2003. "On the construction of blending elements for local partition of unity enriched finite elements." *Int. J. Numer. Methods Eng.* 57 (7): 1015–1038. https://doi.org/10.1002/nme.777.

Dolbow, J., N. Moës, and T. Belytschko. 2000. "Discontinuous enrichment in finite elements with a partition of unity method." *Finite Elem. Anal. Des.* 36 (3–4): 235–260. https://doi.org/10.1016/S0168-874X(00)00035-4.

Dolbow, J., N. Moës, and T. Belytschko. 2001. "An extended finite element method for modeling crack growth with frictional contact." *Comput. Methods Appl. Mech. Eng.* 190 (51–52): 6825–6846. https://doi.org/10.1016/S0045-7825(01)00260-2.

Fries, T.-P. 2008. "A corrected XFEM approximation without problems in blending elements." *Int. J. Numer. Methods Eng.* 75 (5): 503–532. https://doi.org/10.1002/nme.2259.

Fries, T.-P., and T. Belytschko. 2010. "The extended/generalized finite element method: An overview of the method and its applications." *Int. J. Numer. Methods Eng.* 84 (3): 253–304. https://doi.org/10.1002/nme.2914.

Kalthoff, J., and S. Winkler. 1988. "Failure mode transition at high rates of shear loading." In Vol. 1 of *Impact loading and dynamic behavior of materials*. 185–195. Oberursel, Germany: DGM Informationsgesellschaft mbH.

Kim, T. Y., J. Dolbow, and T. Laursen. 2007. "A mortared finite element method for frictional contact on arbitrary interfaces." *Comput. Mech.* 39 (3): 223–235. https://doi.org/10.1007/s00466-005-0019-4.

Leon, S., D. Spring, and G. Paulino. 2014. "Reduction in mesh bias for dynamic fracture using adaptive splitting of polygonal finite elements." *Int. J. Numer. Methods Eng.* 100 (8): 555–576. https://doi.org/10.1002/nme.4744.

Lua, J., T. Zhang, E. Fang, and J.-H. Song. 2016. "Explicit phantom paired shell element approach for crack branching and impact damage prediction of aluminum structures." *Int. J. Impact Eng.* 87 (Jan): 28–43. https://doi.org/10.1016/j.ijimpeng.2015.07.007.

Melenk, J. M., and I. Babuška. 1996. "The partition of unity finite element method: Basic theory and applications." *Comput. Methods Appl. Mech. Eng.* 139 (1–4): 289–314. https://doi.org/10.1016/S0045-7825(96)01087-0.

Menouillard, T., J. Rethore, A. Combescure, and H. Bung. 2006. "Efficient explicit time stepping for the extended finite element method (X-FEM)." *Int. J. Numer. Methods Eng.* 68 (9): 911–939. https://doi.org/10.1002/nme.1718.

Moës, N., J. Dolbow, and T. Belytschko. 1999. "A finite element method for crack growth without remeshing." *Int. J. Numer. Methods Eng.* 46 (1): 131–150. https://doi.org/10.1002/(SICI)1097-0207(19990910)46:13.0.CO;2-J.

Paulino, G. H., K. Park, W. Celes, and R. Espinha. 2010. "Adaptive dynamic cohesive fracture simulation using nodal perturbation and edge-swap operators." *Int. J. Numer. Methods Eng.* 84 (11): 1303–1343. https://doi.org/10.1002/nme.2943.

Rabczuk, T., and T. Belytschko. 2004. "Cracking particles: A simplified meshfree method for arbitrary evolving cracks." *Int. J. Numer. Methods Eng.* 61 (13): 2316–2343. https://doi.org/10.1002/nme.1151.

Rabczuk, T., and T. Belytschko. 2007. "A three-dimensional large deformation meshfree method for arbitrary evolving cracks." *Comput. Methods Appl. Mech. Eng.* 196 (29–30): 2777–2799. https://doi.org/10.1016/j.cma.2006.06.020.

Rabczuk, T., G. Zi, S. Bordas, and H. Nguyen-Xuan. 2010. "A simple and robust three-dimensional cracking-particle method without enrichment." *Comput. Methods Appl. Mech. Eng.* 199 (37–40): 2437–2455. https://doi.org/10.1016/j.cma.2010.03.031.

Rittel, D., R. Levin, and H. Maigre. 1996. "A study of mixed-mode dynamic crack initiation in PMMA." *Mech. Res. Commun.* 23 (5): 475–481. https://doi.org/10.1016/0093-6413(96)00047-X.

Rittel, D., and H. Maigre. 1996. "An investigation of dynamic crack initiation in PMMA." *Mech. Mater.* 23 (3): 229–239. https://doi.org/10.1016/0167-6636(96)00014-2.

Sethian, J. A. 1996. "A fast marching level set method for monotonically advancing fronts." *Proc. Nat. Acad. Sci.* 93 (4): 1591–1595. https://doi.org/10.1073/pnas.93.4.1591.

Soghrati, S., A. M. Aragón, C. Armando Duarte, and P. H. Geubelle. 2012. "An interface-enriched generalized FEM for problems with discontinuous gradient fields." *Int. J. Numer. Methods Eng.* 89 (8): 991–1008. https://doi.org/10.1002/nme.3273.

Song, J.-H., P. M. Areias, and T. Belytschko. 2006. "A method for dynamic crack and shear band propagation with phantom nodes." *Int. J. Numer. Methods Eng.* 67 (6): 868–893. https://doi.org/10.1002/nme.1652.

Song, J.-H., and T. Belytschko. 2009a. "Cracking node method for dynamic fracture with finite elements." *Int. J. Numer. Methods Eng.* 77 (3): 360–385. https://doi.org/10.1002/nme.2415.

Song, J.-H., and T. Belytschko. 2009b. "Dynamic fracture of shells subjected to impulsive loads." *J. Appl. Mech.* 76 (5): 051301. https://doi.org/10.1115/1.3129711.

Song, J.-H., and Y.-C. Yoon. 2014. "Multiscale failure analysis with coarse-grained micro cracks and damage." *Theor. Appl. Fract. Mech.* 72 (Aug): 100–109. https://doi.org/10.1016/j.tafmec.2014.04.005.

Sukumar, N., D. L. Chopp, N. Moës, and T. Belytschko. 2001. "Modeling holes and inclusions by level sets in the extended finite-element method." *Comput. Methods Appl. Mech. Eng.* 190 (46–47): 6183–6200. https://doi.org/10.1016/S0045-7825(01)00215-8.

Sun, H., H. Waisman, and R. Betti. 2014. "A multiscale flaw detection algorithm based on XFEM." *Int. J. Numer. Methods Eng.* 100 (7): 477–503. https://doi.org/10.1002/nme.4741.

Tabarraei, A., J.-H. Song, and H. Waisman. 2013. "A two-scale strong discontinuity approach for evolution of shear bands under dynamic impact loads." *Int. J. Multiscale Comput. Eng.* 11 (6): 543–563. https://doi.org/10.1615/IntJMultCompEng.2013005506.

Ventura, G., E. Budyn, and T. Belytschko. 2003. "Vector level sets for description of propagating cracks in finite elements." *Int. J. Numer. Methods Eng.* 58 (10): 1571–1592. https://doi.org/10.1002/nme.829.

Wang, Y., and H. Waisman. 2017. "Material-dependent crack-tip enrichment functions in XFEM for modeling interfacial cracks in bimaterials." *Int. J. Numer. Methods Eng.* 112 (11): 1495–1518. https://doi.org/10.1002/nme.5566.